Shape-dependent sensitivity of single plasmonic nanoparticles for biosensing

Takumi Sannomiya
Swiss Federal Institute of Technology Zurich
Institute for Biomedical Engineering
Laboratory of Biosensors and Bioelectronics
Gloriastrasse 35
Zurich, 8092 Switzerland

Christian Hafner
Swiss Federal Institute of Technology Zurich
Department of Information Technology
and Electrical Engineering
Laboratory for Electromagnetic Fields
and Microwave Electronics
Gloriastrasse 35
Zurich, 8092 Switzerland

Janos Vörös
Swiss Federal Institute of Technology Zurich
Institute for Biomedical Engineering
Laboratory of Biosensors and Bioelectronics
Gloriastrasse 35
Zurich, 8092 Switzerland

Abstract. Shape-dependent sensitivity of localized surface plasmon–based biosensing was investigated by combining single-particle protein-sensing and multiple multipole program simulation. Significantly higher sensitivity was observed for tetrahedral particles than spherical ones, which was revealed by careful structural analysis of individually measured particles. The simulation of the corresponding particles with layered protein adsorption model showed consistent optical property and sensitivity, which were explained in terms of the field enhancement at the pointing edges. © *2009 Society of Photo-Optical Instrumentation Engineers.* [DOI: 10.1117/1.3269678]

Keywords: localized surface plasmon resonance; biosensor; electromagnetic simulation; multiple multipole program.

Paper 09248PR received Jun. 15, 2009; revised manuscript received Sep. 3, 2009; accepted for publication Oct. 6, 2009; published online Dec. 7, 2009.

1 Introduction

Plasmonic metallic nanoparticles are drawing great attention due to their strong field enhancement at the close vicinity of the surface and to their unique optical resonances. Nanoparticles made of noble metal exhibit strong optical resonances at visible wavelengths, so-called localized surface plasmon resonances (LSPR), which are dependent not only on the material and geometry of the particles but also on the refractive index of the surroundings. One of the most promising applications is an optical biosensor.[1–3] In such plasmonic biosensors, the noble metal nanoparticles are functionalized by receptor molecules to sense target ligands, which are typically proteins. Because proteins have higher refractive index than aqueous solution, their adsorption changes the refractive index in the vicinity of the nanoparticles, inducing a shift in the LSPR peak.[1–3] This simple detection principle is a great advantage to miniaturize the system and realize multiplexed high-throughput assay.[4,5] When the plasmonic structure is tuned up and the signal is properly processed, high sensitivity comparable to or even better than other existing methods can be realized despite its simple detection methodology and small detection area.[6,7] As the ultimate sensing scale, single binding events were recently observed using single-particle signal transducers.[8]

On one hand, this simple sensing principle is a strong advantage of LSPR-based sensing. On the other hand, LSPR is a complicated phenomenon: the peak position and its sensitivity to the surrounding refractive index change are greatly dependent on the shape, size, and material of the plasmonic particles and even on the molecular adsorption position.[8–10] In order to understand such complex LSPR phenomena and to engineer sensitive LSPR sensors, a combinatory approach of experiments and numerical simulation is essential.

There are various numerical simulation methods for plasmonic structures. Volume discretization methods, such as finite difference time domain (FDTD) method and finite element method (FEM), are often used due to their relatively easy and intuitive handling of the software. However, volume discretization methods require extremely fine meshes in plasmonic structures to achieve a reliable result with decent accuracy, which has huge memory need and requires long computation time.[11,12] In this study, we used the latest version of the multiple multipole program (MMP) contained in the MaX-1 software package.[13] MMP is based on a semianalytic boundary method where the field is expressed by the sum of distributed analytical solutions of Maxwell's equations.[13,14] This program is not only accurate but also has various advantages to facilitate the computation, such as symmetry decomposition to reduce the computational load.[15]

When comparing the experimental results and simulation, it is more informative to investigate individual single particles than measuring the average of millions of particles as the distribution of the shape and size of the particles blurs out the information. Therefore, to take the most advantage of simulation, the experimental part of this study centers on single-particle sensing and the structural analysis of each particle. There has been several studies on single-particle sensors,

Address all correspondence to: Takumi Sannomiya. Swiss Federal Institute of Technology Zurich, Institute for Biomedical Engineering, Laboratory of Biosensors and Bioelectronics Gloriastrasse 35, Zurich, 8092, Switzerland. Tel: 41 44 632 57871; Fax: 41 44 632 1193; E-mail: sannomiya@biomed.ee.ethz.ch

1083-3668/2009/14(6)/064027/6/$25.00 © 2009 SPIE

claiming the small sensing amount.[16–18] However, the diversity of the particle shape and size, which is less problematic for average measurement, risks the reproducibility unless the same particle is always followed or good statistics are taken.[19] The real advantage of single-particle analysis is to be able to confirm such diversity and to pick up different information from each particle by observing the same single particles.[8,20,21] When exactly the same single particles are observed in all the measurements, no statistical fluctuation from the fabrication would be involved, which therefore leads to more reliable analysis.

In this paper, we first present the experimental single-particle biosensing and the observation of the individual measured particle shapes. Simulations, based on the experimental structural analysis, are demonstrated to study shape-dependent optical property and sensitivity. Experimental and simulated results are then compared and discussed in terms of sensitivity and field enhancement.

2 Method

2.1 *Experimental*

Colloidal gold particles with diameter of 100 nm were purchased from British Biocell (GC100). A diluted solution of gold colloid was directly deposited on a glass substrate with well-separated interparticle distances to measure the spectra from individual single particles. The deposited particles were physically bound to the glass substrate stable enough for water rinsing and a drying process by nitrogen blow. The measured particles had interparticle distances of >2 μm from the neighboring particles, which is enough to avoid interparticle optical coupling.

A dark-field microscope (Axiovert 200, Carl Zeiss, Gottingen, Germany) equipped with a spectrophotometer (SpectraPro 2150, PIXIS 400, Princeton Instruments, Trenton, NJ, USA) was used to measure the scattering spectra. Numerical aperture (NA) of the illumination was 0.8–0.95, and NA of the objective 0.4. These correspond to the illumination angle of 53–72 deg and the detection angle within 24 deg in ambient condition. The measurement was performed in aqueous condition in a flow cell. A halogen lamp (100 W) was used for illumination. Kinetic measurements were recorded and evaluated by a custom-made program that can eliminate the effect of focus-dependent peak shifts.

The molecular adsorption measurements were conducted using a 160-mM buffer solution consisting of 10 mM 4-(2-hydroxyethyl)piperazine-1-ethanesulfonicacid with 150 mM NaCl, adjusted to pH 7.4 (HEPES). The concentration of the Immunoglobulin G (IgG) for the protein adsorption measurements was 100 μg/mL.

In this particular measurement set, we measured seven particles simultaneously and selected the largest, a midsized, and the smallest spherical particles, and a tetrahedral one, as representatives in this paper. Including separate measurement sets, we observed over 17 particles and basically saw the same effect, which will be described in the following sections.

A scanning transmission microscope [(SEM), Supra 50VP, Carl Zeiss, Germany] was used to observe the shape of the particles. The samples were coated with amorphous carbon for conductivity required for SEM imaging. All the images were taken at the acceleration voltage of 5 kV by an in-lens secondary electron detector. The same particles as the optical dark-field imaging were identified by comparing the orientation of the particles at low magnification with the previously taken optical dark-field images.

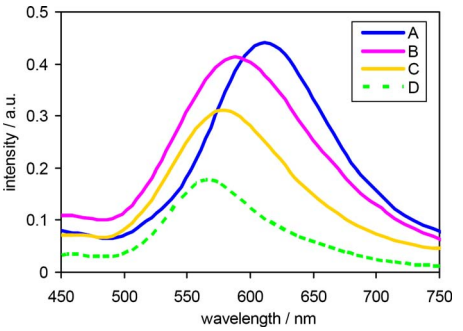

Fig. 1 Experimental scattering spectra of four individual gold particles.

2.2 *Simulation*

When the size of a plasmonic particle is <150 nm and the illuminated wavelength is around visible, dipolar oscillation mode is dominant and, therefore, s-scattering is dominant.[8] To calculate the scattering intensity, we measured 90 deg s-scattering at 2 μm away from the scattering object, where the evanescent component is negligible. We approximated all the particles as solids of rotation, and the illuminating plane wave was along the symmetry axis in order to take advantage of symmetry decomposition: only the first Fourier component [cos(1) type] around the symmetry axis should be considered for the (ring-)multipole expansions on the symmetry axis. The matching point slices are set at 45 deg from the electric- and magnetic-field vector of the excitation plane wave to include both components. Such treatment of symmetry decomposition reduces the virtual dimension of the 3-D problem to 2-D.[15] The maximum relative error at the matching point was always $<0.5\%$.

For the dielectric constant of gold, measured data by Johnson and Christy were used.[22] The dielectric constants of solution and the protein adsorption layer were considered to be real and constant as the value of 1.777 ($n=1.333$) and 2.1 ($n=1.45$), respectively.

3 Results

3.1 *Spectra and Adsorption Kinetics*

Figure 1 shows experimentally acquired scattering spectra of four individual gold nanoparticles in the buffer solution. LSPR peaks are observed around the wavelength of 600 nm. Particles A (blue) and B (pink) exhibited similar resonance intensities while the peak position of particle A is more red-shifted than B. The spectral shape of particles C and D is similar to that of B with smaller intensities and more blue-shifted resonance position.

These four particles were used for a sensitivity test. The resonance peak shifts were plotted as functions of time in Fig. 2 to see the kinetics of the protein adsorption. The protein injections were conducted at 5, 300, 600, 2500, 2800 and 3200 s and rinsing with buffer solution at 950 and 2000 s. All

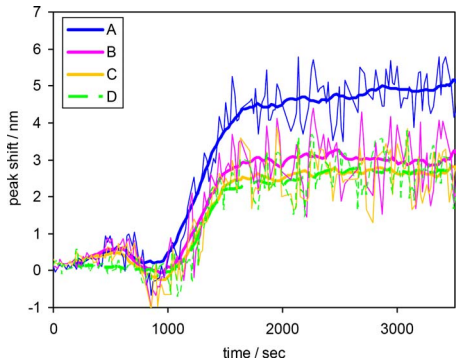

Fig. 2 Adsorption kinetics of IgG (100 μg/mL) on four individual particles of Fig. 1. Peak shift of each particle is plotted as a function of time. The thin lines represent the raw data. Smoothed data (thick lines) are superimposed to guide the eye. Rinsing was conducted at 5, 300, 600, 2500, 2800 and 3200 s by buffer solution, and at 950 and 2000 s by IgG solution.

four particles showed redshift of the resonance when protein molecules were injected, which saturated after a few minutes of adsorption. The redshift remained same after rinsing by buffer, confirming the sensing of the expected irreversible adsorption of proteins. Interestingly, particle A exhibited larger peak shift than the other three particles.

3.2 *SEM Observation*

We observed the four particles used for sensing by SEM. Figure 3 shows SEM images and corresponding optical dark-field images (insets), which confirm that same particles were observed in the optical measurements and in SEM. The measured particles are indicated by circles. Even after sample washing by water, drying, and subsequent carbon coating, the particles remained at the same position. The magnified SEM images of these particles are shown in Fig. 4. The particles were imaged at different observation angles to clarify the 3-D shape of each particle. The image in the center corresponds to the observation angle normal to the substrate plane. The surrounded four images were taken at the zenithal angle of 30 deg with different azimuthal angles with 90 deg steps. A schematic of the observation condition is shown in Fig. 4(e).

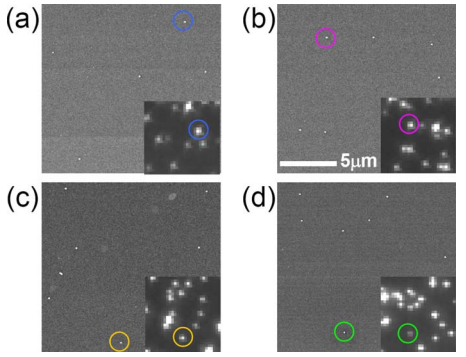

Fig. 3 SEM images and corresponding optical darkfield images (inset) of four measured particles to verify the same observation position. The measured particles are indicated by circles. The color of the indication circle and the numbering correspond to Figs. 1 and 2.

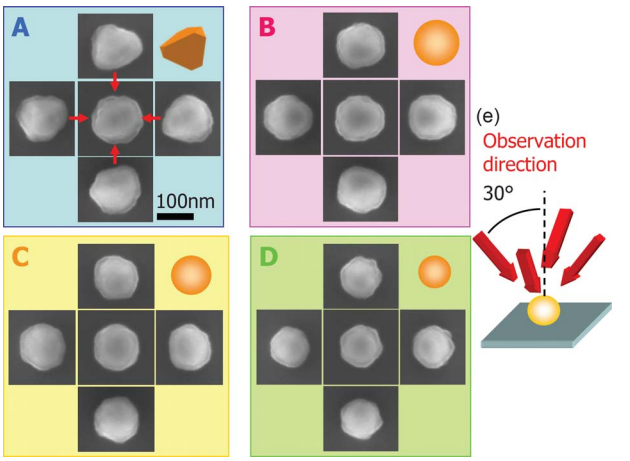

Fig. 4 Magnified SEM images of the four particles with different observation angles. The observation angles are schematized in (e).

The SEM images at different observation angles revealed that particle A was actually not spherical but tetrahedral because it looks triangular, square, and hexagonal, depending on the observation angles. On the other hand, the other three particles have rather spherical shapes. The sizes of the spherical particles B, C, and D are roughly estimated as 100, 90, and 80 nm, respectively. It should be noted that the particles were coated by carbon, which makes the particles appear larger with complicated contrast effects at the edges.

3.3 *Simulated Spectra and Sensitivity*

On the basis of the SEM images, we have modeled the particles with different sizes and shapes: namely, sphere, rotated triangle, and rotated rhomboid with rounded edges. (See schematics in Figs. 5 and 6.) We expected that the cone-shape particle (rotated triangle) emulates the tetrahedral particle A in the experiment. The sizes of the spherical particles were set to be 100, 90, and 80 nm, which are equal to the estimated sizes of particles B, C, and D in the experiment. For comparison, a rotated rhomboidal particle was also simulated. The volume and surface area of the simulated particles are summarized in Table 1. The simulated scattering spectra of these particles are shown in Fig. 5. The shapes of nonspherical particles are also

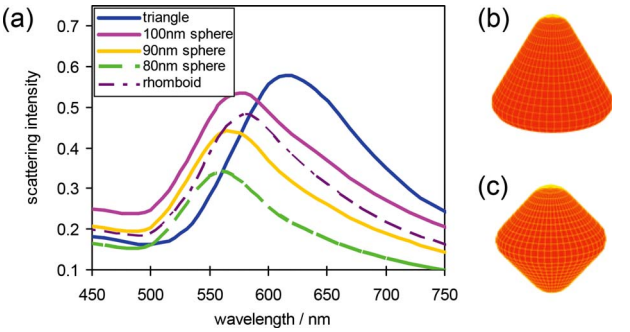

Fig. 5 (a) Simulated spectra of gold particles with different sizes and shapes. The illustration (b,c) describes the simulated (b) rotated-triangle-shaped particle and (c) rotated-rhomboid-shaped particle.

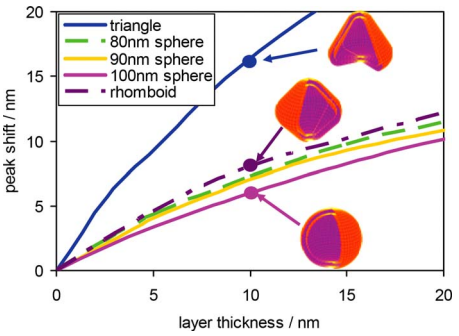

Fig. 6 Simulated peak-shift plot as a function of layer thickness. Layer models at the thickness of 10 nm are shown for triangle, 100 nm sphere, and rhomboid particles.

Table 1 Volume, surface area, and electric-field enhancement factor of the simulated particles. The electric-field enhancement factors are extracted from the field pattern at the resonance as in Fig. 6.

	Volume (10^5 nm^3)	Surface area (10^4 nm^2)	Electric-field enhancement
Triangle	4.1	3.1	16.7
100-nm Sphere	5.2	3.1	7.0
90-nm Sphere	3.8	2.5	7.3
80-nm Sphere	2.7	2.0	7.5
Rhomboid	3.7	2.6	12.7

shown in Fig. 5(b) and 5(c). Triangular particle gives higher and redshifted resonance peak compared to other particles.

The electric-field patterns of these particles at their resonance wavelength are shown in Fig. 7. Only the cross sections along the excitation electric-field vector are shown. Clearly, the pointing edges of the triangular particle and the rhomboid particle accumulate the energy and create stronger field than spherical particles. The field enhancement factors (strongest field/illumination field) are also listed in Table 1.

To estimate the sensitivity as a biosensor, we covered the particle with a solid layer with higher refractive index. The layer thickness was varied, and the peak shift was monitored same as in the experiment of Fig. 2. Figure 6 shows the peak-shift plots as functions of the layer thickness. As the layer thickness increases, the peak shift also increases in the positive direction. In terms of peak shift, the triangular particle is more sensitive than the other particles. The largest spherical particle showed least sensitivity among the simulated particles.

4 Discussion

4.1 *Spectra and Field Enhancement*

It is quite well known that rod-shaped or facetted particles show more redshifted LSPR peaks.[1,9,23] The redshift of resonance can be explained by easier polarization of pointy structures. The redshifted resonance of particle A compared to spherical particles in Fig. 1 is due to the pointy structure of tetrahedral shape as seen in Fig. 4. We expected that the triangle particle in the simulation emulates particle A. Indeed, the simulated spectrum of the triangle particle well reproduced that of particle A of the experiment (Figs. 1 and 5). The scattering spectra of all the four measured particles were nicely represented by simulated triangular and spherical particles. Actually, the substrate, which is not included in the simulation, can affect the peak position when the edge of the particle is pointing toward the substrate because the enhanced field would sense the substrate stronger than spherical particles (see field patterns of Fig. 7).

The triangular particle in the simulation exhibits higher scattering intensity at the resonance than the spherical 100-nm particle despite its smaller volume. This is probably due to the stronger polarization of the particle. The field enhancement factor of the triangle particle is indeed stronger, which is clearly shown also in the field pattern in Fig. 7. The simulated rhomboid particle has equivalent volume and surface area to the 90-nm spherical particle (Table 1), which implies a small difference in shape. Nevertheless, it gives stronger scattering intensity (Fig. 5) and stronger field enhancement (Fig. 6 and Table 1) by the pointing structure. The

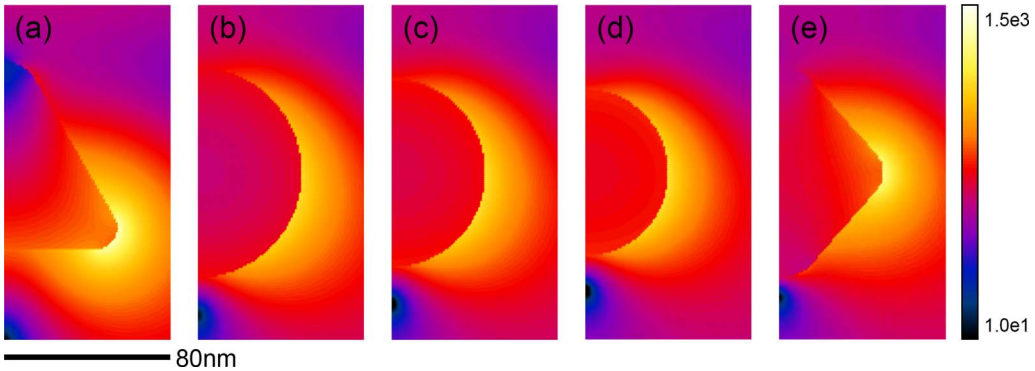

Fig. 7 Simulated electric-field patterns of the cross section along the excitation electric-field vector of the five simulated particles at their resonance wavelengths: (a) triangular at $\lambda = 615$ nm, (b) 100 nm sphere at $\lambda = 559$ nm, (c) 90 nm sphere at $\lambda = 567$ nm, (d) 100 nm sphere at $\lambda = 576$ nm, and (e) rhomboid $\lambda = 580$ nm. The intensity of the electric field is scaled logarithmically in the color scheme.

field enhancement factor of spherical particles is higher for smaller particles. Similar to the pointing structure, the curvature plays a role to accumulate the field for spherical particles.

4.2 *Sensitivity*

The tetrahedral shaped particle A performed a bigger peak shift upon protein adsorption than the other spherical particles, as seen in Fig. 2. The simulated sensitivity of the equivalent triangular particle shows coherent results in Fig. 7. The signal multiplication from the spherical particle is roughly factor of 2. There are only minor differences in the sensitivity among the spherical particles both in the measurement and simulation. The simulated rhomboidal particle showed slightly better sensitivity than spherical particles. These suggest a direct correlation between the sensitivity and the field enhancement factor.

Looking more into the details of the results with the spherical particles, the sensitivity of the 100-nm particle in the experiment and simulation gives an opposite relation regarding the particle size. This is probably due to the imperfect spherical shape of the real particles. A larger particle tends to have more facets by crystalline growth with pointing edges, which would compensate its intrinsically lower sensitivity of the larger particle by a more enhanced field at the pointing edges.[24]

The protein layer of IgG molecule is expected to have 5–15 nm thickness considering the molecular size.[7,25] However, the magnitude of the peak shift by IgG adsorption in the experiment is considerably less than the expected peak shift of 5–15 nm layer in the simulation. This difference probably originates from the unrealistically sharp well-defined boundary of the protein layer in the simulation. Non-negligible scattering happens at the protein-water boundary. In reality, the boundary of the protein layer is most likely diffuse, giving suppressed scattering at the protein-water boundary. The substrate would also reduce the sensitivity especially for the triangular (tetrahedral) particle as discussed above.

5 Conclusions

Single-particle LSPR biosensing was demonstrated along with the structural analysis of the individually measured particles. Compared to the spherical particles, the tetrahedral particle showed redshifted resonance and better sensitivity upon protein adsorption. These experimental results were supported and well explained by MMP simulation in terms of field enhancement. MMP analysis further implied that a slight modification of the shape, especially with pointing structure, can enhance the LSPR signal intensity, accumulated field, and sensitivity as a biosensor.

The possibility to follow the same particles throughout all measurement procedures is highly beneficial because the individual fabrication error of each particle, such as size and shape diversity, can be included in the analysis, while the averaged measurement with numbers of particles can only be treated statistically. This advantage becomes important especially during simulation-based quantification attempts because the model must have a defined dimension, and it is difficult to account for the statistical fluctuations.

A single-nanoparticle-based biosensor is ultimately the smallest sensing element, probably among all the existing biosensing methods. Such sensing by single nanoscaled plasmonic structures could enable extremely fast screening of a dense array of elements for multiplexing, which can be compared to the memory bit in magnetic recording. However, its realization in practical applications, especially the integration of plasmonic sensing elements into CMOS-based microelectronic devices, requires further development.

Acknowledgments

This study is funded by ETH Zürich.

References

1. A. J. Haes, D. A. Stuart, S. Nie, and R. P. Van Duyne, "Using solution-phase nanoparticles, surface-confined nanoparticle arrays and single nanoparticles as biological sensing platforms," *J. Fluoresc.* **14**(4), 355–367 (2004).
2. J. R. Lakowicz, "Plasmonics in biology and plasmon-controlled fluorescence," *Plasmonics* **1**, 5–33 (2006).
3. P. K. Jain, X. Huang, I. H. El-Sayed, and M. A. El-Sayed, "Review of some interesting surface plasmon resonance-enhanced properties of noble metal nanoparticles and their applications to biosystems," *Plasmonics* **2**, 107–118 (2007).
4. P. Neuzil, and J. Reboud, "Palm-sized biodetection system based on localized surface plasmon resonance," *Anal. Chem.* **80**, 6100–6103 (2008).
5. N. C. Lindquist, A. Lesuffleur, H. Im, and S. H. Oh, "Sub-micron resolution surface plasmon resonance imaging enabled by nanohole arrays with surrounding Bragg mirrors for enhanced sensitivity and isolation," *Lab Chip* **9**, 382–387 (2009).
6. A. B. Dahlin, J. O. Tegenfeldt, and F. Hook, "Improving the instrumental resolution of sensors based on localized surface plasmon resonance," *Anal. Chem.* **78**, 4416–4423 (2006).
7. T. Sannomiya, P. K. Sahoo, D. I. Mahcicek, H. H. Solak, Ch. Hafner, D. Grieshaber, and J. Voros, "Biosensing by densely packed and optically coupled plasmonic particle arrays," *Small* **5**, 1889–1896 (2009).
8. T. Sannomiya, Ch. Hafner, and J. Voros, "*In-situ* sensing of single binding events by localized surface plasmon resonance," *Nano Lett.* **8**, 3450–3455 (2008).
9. S. Link, and M. A. El-Sayed, "Spectral properties and relaxation dynamics of surface plasmon electronic oscillations in gold and silver nanodots and nanorods," *J. Phys. Chem. B* **103**, 8410–8426 (1999).
10. K. A. Willets and R. P. Van Duyne, "Localized surface plasmon resonance spectroscopy and sensing," *Annu. Rev. Phys. Chem.* **58**, 267–297 (2007).
11. J. Smajic, Ch. Hafner, L. Raguin, K. Tavzarashvili, and M. Mishrikey, "Comparison of numerical methods for the analysis of plasmonic structures," *J. Comput. Theor. Nanosci.* **6**, 1–12 (2009).
12. A. Taflove and S. C. Hagness, *Computational Electrodynamics: The Finite-Difference Time-Domain Method*, Artech House, Boston (2005).
13. Ch. Hafner, *MaX-1: A Visual Electromagnetics Platform*, Wiley, Chichester, UK (1998).
14. Ch. Hafner, "Boundary methods for optical nano structures," *Phys. Status Solidi B* **244**, 3435–3447 (2007).
15. T. Sannomiya, J. Voros, and Ch. Hafner, "Symmetry decomposed MMP calculation of plasmonic particles on substrate for biosensing applications," *J. Comput. Theor. Nanosci.* **6**, 749–756 (2009).
16. G. Raschke, S. Kowarik, T. Franzl, C. Sonnichsen, T. A. Klar, J. Feldmann, A. Nichtl, and K. Ku1rzinger, "Biomolecular recognition based on single gold nanoparticle light scattering," *Nano Lett.* **3**(7), 935–938 (2003).
17. A. D. McFarland, and R. P. Van Duyne, "Single silver nanoparticles as real-time optical sensors with zeptomole sensitivity," *Nano Lett.* **3**(8), 1057–1062 (2003).
18. G. J. Nusz, S. M. Marinakos, A. C. Curry, A. Dahlin, F. Hook, A. Wax, and A. Chilkoti, "Label-free plasmonic detection of biomolecular binding by a single gold nanorod," *Anal. Chem.* **80**, 984–989 (2008).
19. C. L. Baciu, J. Becker, A. Janshoff, and C. Sonnichsen, "Protein-membrane interaction probed by single plasmonic nanoparticles,"

Nano Lett. **8**(6), 1724–1728 (2008).
20. C. L. Nehl, H. Liao, and J. H. Hafner, "Optical properties of star-shaped gold nanoparticles," *Nano Lett.* **6**(4), 683–688 (2006).
21. A. Unger, U. Rietzler, R. Berger, and M. Kreiter, "Sensitivity of crescent-shaped metal nanoparticles to attachment of dielectric colloids," *Nano Lett.* **9**, 2311–2315 (2009).
22. P. Johnson, and R. Christy, "Optical constants of the noble metals," *Phys. Rev. B* **6**, 4370–4379 (1972).
23. W. A. Murray and W. L. Barnes, "Plasmonic materials," *Adv. Mater.* **19**, 3771–3782 (2007).
24. M. Grzelczak, J. Perez-Juste, P. Mulvaney, and L. M. Liz-Marza, "Shape control in gold nanoparticle synthesis," *Chem. Soc. Rev.* **37**, 1783–1791 (2008).
25. L. J. Harris, E. Skaletsky, and A. McPherson, "Crystallographic structure of an intact IgG1 monoclonal antibody," *J. Mol. Biol.* **275**, 861–872 (1998).